

Velocity Distributions in Magnetron Sputter

C. H. Shon, J. K. Lee, H. J. Lee, Y. Yang, and T. H. Chung

Abstract— Results of the particle simulation of magnetron sputter are presented. Using a kinetic code, we obtain the spatial profiles of plasma density, potential, and velocity distribution function, along with the electron temperature, the ion density, the current density, and the deposition profiles at the anode surface. The result of simulation is compared with the Child–Langmuir law applied to the magnetron discharge and the global model. The velocity distribution function of electrons is Maxwellian, but that of ions is non-Maxwellian near the cathode with the majority in the energy range below 50 eV.

Index Terms— Kinetic simulation, magnetron, sheath, sputter, velocity distribution.

I. INTRODUCTION

PLANAR magnetron sputter [1]–[6] is widely used as a plasma processing device. The field of application is sputter deposition [7], reactive sputter deposition, reactive ion etching, and coating of thin films. Taking the advantage of magnetic field, magnetron sputter operates at a low pressure and a low voltage.

Applied magnetic field confines energetic electrons near the cathode. These confined electrons ionize neutral gas and form high density plasma near the cathode surface. Ions produced by these electrons are accelerated toward the cathode surface with high energy. This bombardment of ions not only sputters out target materials, but also produces secondary electrons which maintain discharge.

As the microelectronics industry grows exponentially, fabrication of thin film process becomes a crucial point of concern. Many research activities about magnetron sputter have been carried out by experimental methods but not much by theory and simulation. Numerical simulation and theory generate realistic and useful results. There are three-dimensional (3-D) particle-in-cell/Monte Carlo (PIC/MC) simulation results [8], [9] which are computationally costly. Thus we use a PIC/MC two-dimensional (2-D) simulation code OOPIC [10].

In Section II, the simulation results are shown for the magnetron geometry and the breakdown characteristics in Section II-A for the profiles of the plasma quantities in Section II-B and for the velocity distributions of electrons and ions in Section II-C. The steady-state property is discussed in Section III, and the summary with a conclusion is given in Section IV.

Manuscript received February 6, 1998; revised August 7, 1998. This work was supported in part by LG Electronics, the Basic Science Research Institute Program, Ministry of Education 1997, Project 97-2439, and POSTECH/BSRI Special Fund.

C. H. Shon, J. K. Lee, H. J. Lee, and Y. Yang are with the Pohang University of Science and Technology, Pohang 790-784, South Korea (e-mail: jkl@postech.ac.kr).

T. H. Chung is with the Dong-A University, Pusan 604-714, South Korea. Publisher Item Identifier S 0093-3813(98)09635-0.

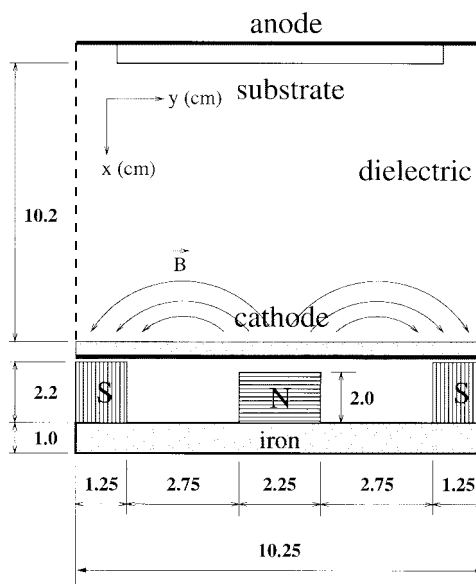


Fig. 1. Schematic diagram of magnetron sputter used in the simulation.

II. SIMULATION RESULTS

A. Geometry and Breakdown of Discharge

The schematic geometry of magnetron sputter used in our simulation is shown at Fig. 1. The simulation region is the square with L_x of 10.2 cm and L_y of 10.25 cm. Magnets are located behind the cathode. L_x is the distance between the anode at $x = 0$ and the cathode at $x = L_x$. Other boundary is closed with dielectric material. There is also iron plate below permanent magnets. Magnetic fields are calculated with the POISSON code [11]. Using this magnetic field, we simulate with a particle code OOPIC [10]. Shown in Fig. 2 is the input magnetic field for the OOPIC code. Various magnet geometries can be used to determine the optimum geometry for magnetron sputter.

The breakdown curve for the magnetron-sputter geometry is shown in Fig. 3. The dotted line indicates the theoretical curve for unmagnetized cases (the Paschen curve), and the solid curve shows our simulation results for the magnetized case using the magnetic field as in Figs. 1 and 2. It also shows that much lower pressure can be used for breakdown at the same size of geometry and at much lower voltage. These beneficial effects are due to the magnetic field. The applied magnetic field traps electrons to increase their number density, which increases the ion density by ionizing the neutral gas. This leads to higher ion bombardment and higher sputtering rates at the cathode target. Voltage and pressure change affect plasma properties. Plasma density increases with increased pressure or voltage.

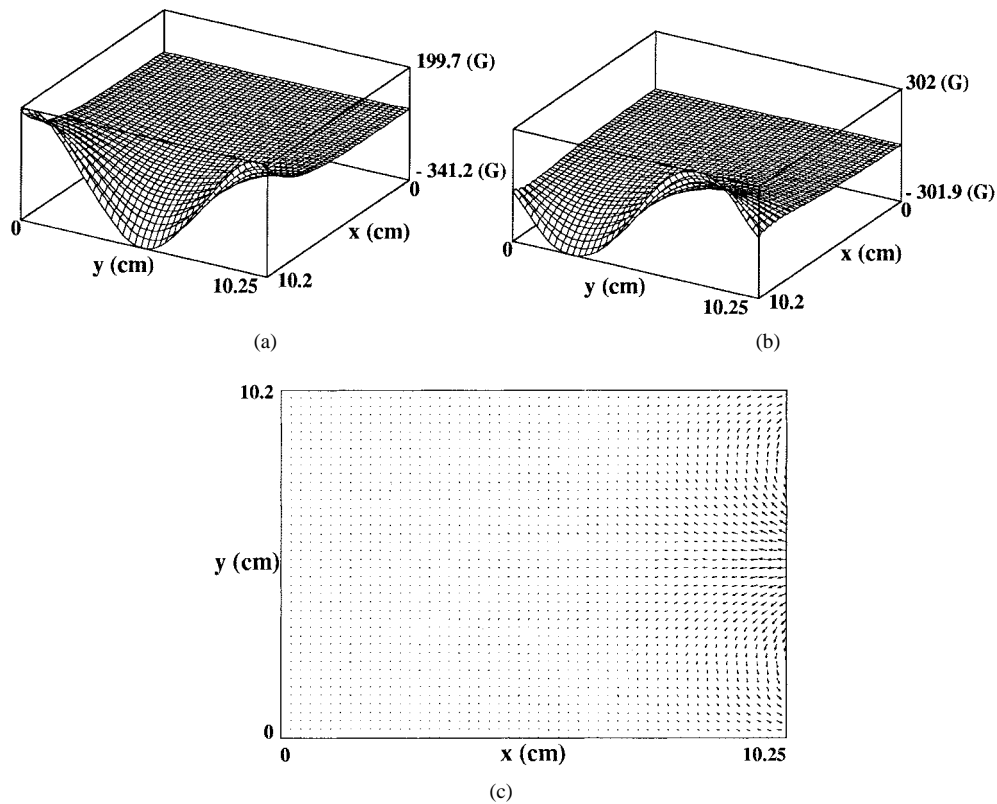


Fig. 2. Magnetic field distribution used in OOPIC for the strength of (a) B_x , (b) B_y in Gauss, and (c) the total B-field vector.

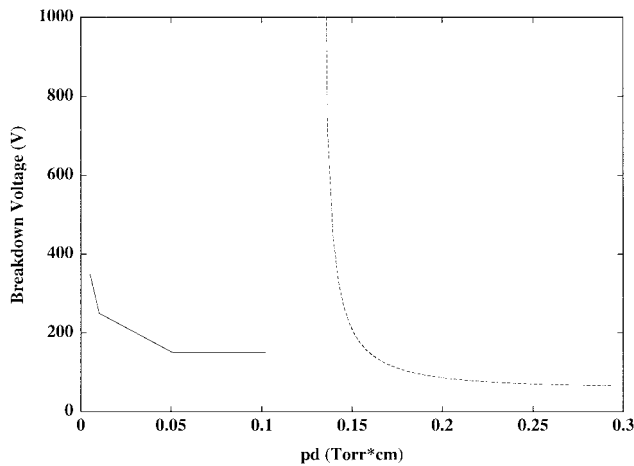


Fig. 3. Breakdown curve for a given magnetron geometry. Dotted line is the theoretical curve for an unmagnetized plasma, and solid line is the breakdown curve for our magnetron sputter.

B. Profiles of Plasma Characteristics

Out of more than a dozen simulations, our typical simulation uses Ar gas with the pressure 5 mtorr and the applied potential 400 V. The highest magnetic field is 302 Gauss at the cathode surface between N and S poles. Typical results of OOPIC simulation for our geometry are shown in Fig. 4 for the number, the potential, the electron and the ion density-profiles. These values are taken at 3×10^{-6} s which is approximately seven times the ion plasma period. These profiles do not change significantly during this time, thus considered approaching the steady state. At 3×10^{-6} s, we obtain the same order

of peak density of electrons and ions to those of Nanbu [8] and [9]. Although the steady state is not reached because of prohibitively high computing costs, our results show the important profile and velocity characteristics near the steady state. The electric field in the sheath region shows a linear slope in our simulations, which means that the ion distribution is uniform in this region to make a matrix sheath. A laser induced fluorescence (LIF) experiment shows the similar results [6].

The particle distribution in x - y space is shown in Fig. 5(a) and (b), and the phase-space distribution in Fig. 6. Electrons are confined along magnetic field lines. Plasma density is higher where the magnetic field is parallel to the cathode surface. The density peak coincides with the $B_x = 0$ points. Near the anode, the particle distribution becomes more uniform. Sheath size of our system is approximately 2 mm at 3×10^{-6} s. Phase-space plots show useful information. Electrons are distributed in the region where the magnetic field is high. A sheath region forms near the cathode, where electrons are rare. Ion distribution shows that there are many particles in the lower energy region. Ion velocity is increasing toward the cathode.

Ion density at the cathode surface, the current density calculated from the velocity distribution at the cathode, and the deposition profile at the substrate are shown in Fig. 7(a) at $t = 2 \times 10^{-6}$ s and (b) at $t = 3 \times 10^{-6}$ s. The above quantities are normalized. We note that the peaks of the ion density and the current density do not change in time significantly. The deposition profile which depends on the magnetic field shape and the geometry of magnetron sputter is calculated with an assumption that the sputtered atoms from the target surface are

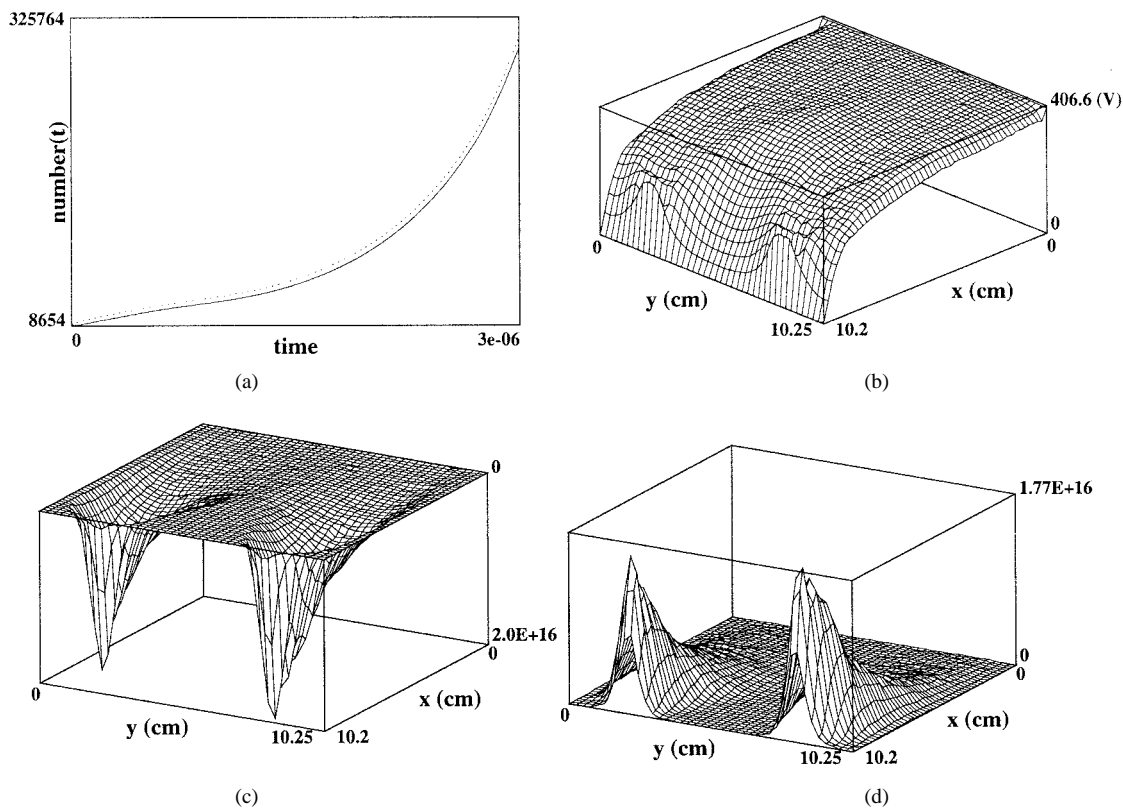


Fig. 4. Simulation results at 3×10^{-6} s, $p = 5$ mtorr, and $V = 400$ V. (a) Total number density, (b) potential, (c) electron number density, and (d) Ar ion number density.

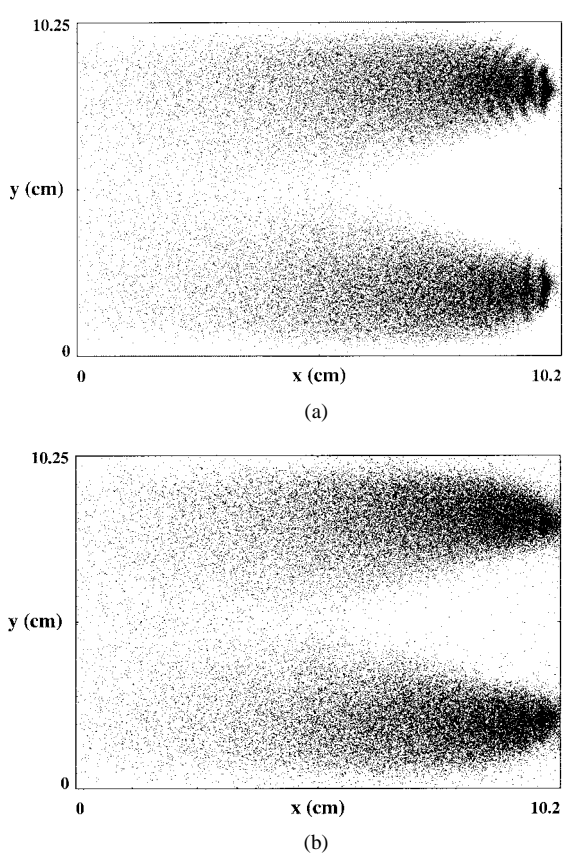


Fig. 5. The particle distribution of (a) electrons and (b) ions in x - y space.

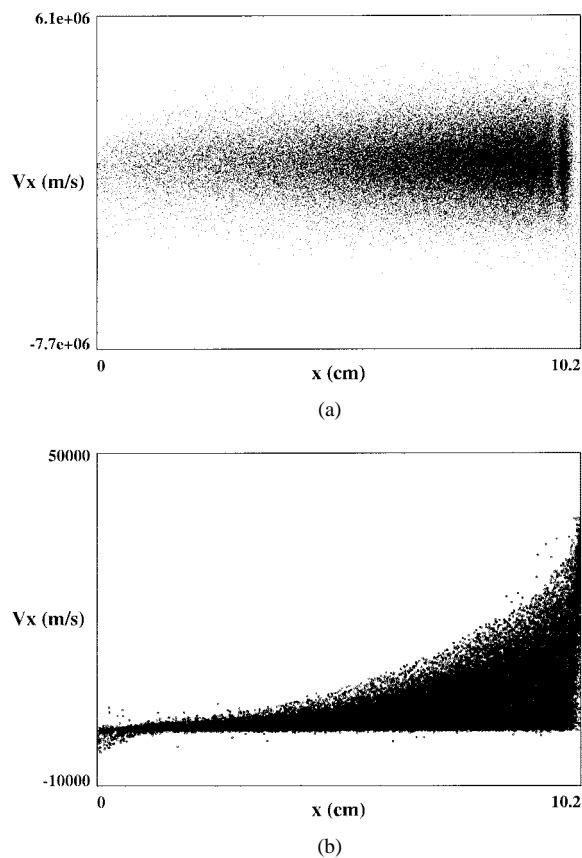


Fig. 6. The phase-space velocity distributions of (a) electrons and (b) ions.

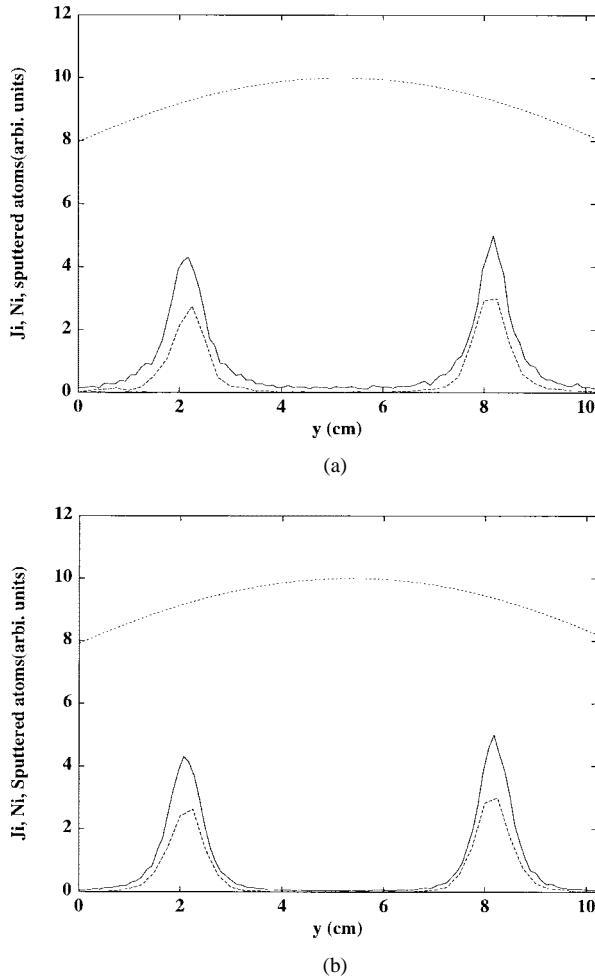


Fig. 7. Ion density at the cathode surface (the lower dotted line), the current density at the cathode (solid line), and the deposition profiles at the substrate (the upper dotted line) at (a) $t = 2 \times 10^{-6}$ s and (b) $t = 3 \times 10^{-6}$ s.

scattered isotropically to reach the substrate without engaging collisions with neutral gas. Motohiro [13]–[15] and Somekh [16] simulate the flight of sputtered atoms using an MC scheme. They take into account thermalization of energetic atoms by collision between sputtered atoms and neutral gas, which is ignored in our calculation.

Other results using different magnetic fields and geometries are shown Fig. 8. As the peak points are shifted toward the edges, the deposited atom density at the anode substrate is flattened for an optimized deposition profile. Cathode erosion profile also can be obtained from these ion density and current density profiles at the cathode. The uniformity of the deposited atom density and the cathode erosion profile are important in plasma processing. Geometry and sputtering condition can be optimized by simulation.

C. Velocity Distributions

Electron and ion velocity distributions are important and useful for many practical purposes. In Fig. 9, the velocity distribution functions of electrons and ions at the cathode are shown. Fig. 9(a), (c), and (e) is the electron velocity distributions at the cathode surface for the x , y , and z com-

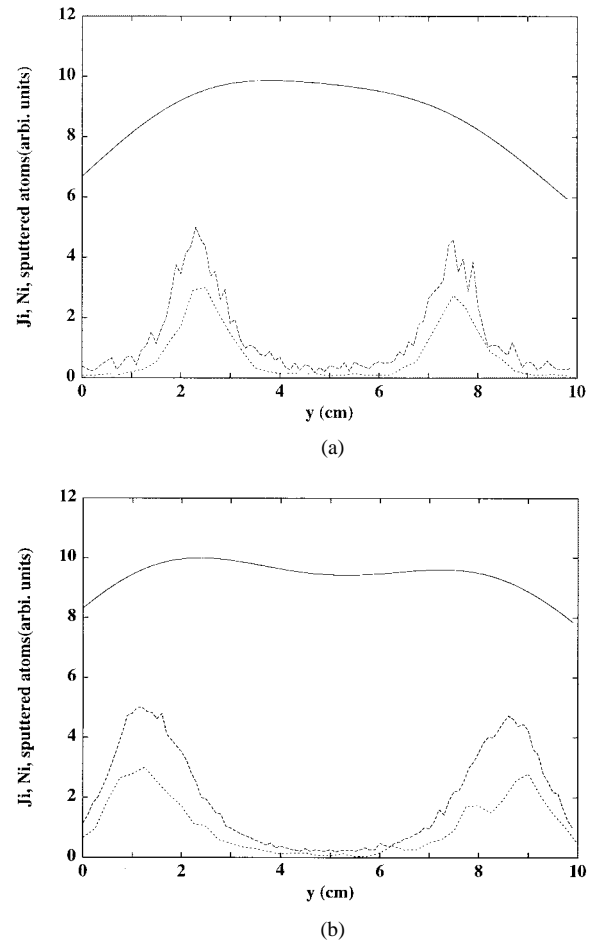


Fig. 8. Ion density at the cathode surface (lower dotted line), the current density at the cathode (the solid line), and the deposition profile at the substrate (the upper dotted line) with (a) a narrow gap between density peak and (b) a broad gap between density peak due to different magnetron geometry.

ponents of the electron velocity. Fig. 9(b), (d), and (f) is the ion velocity distributions at the cathode surface for the x , y , and z components of the ion velocity. Ions have finite velocities along the x direction, while other components of the velocities are not significantly different from zero. We calculate the current density of ions entering cathode from these distributions using

$$J_d = eN_iV_i \quad (1)$$

where N_i is ion density at the cathode and V_i is the ion velocity toward the cathode surface.

Plasma distribution is Maxwellian in the bulk region. Near the boundary, a sheath region exists and a highly non-Maxwellian distribution appears. Fluid theory is valid when the plasma distribution is Maxwellian. There are many attempts to analyze the sheath region of sputter using fluid theory assuming Maxwellian distribution [17]–[20].

In our particle simulation, we obtain electron and ion velocity distributions. We calculate the particle distribution in a given region at a specified x location. Figs. 10 and 12 are the electron and ion velocity distributions in front of

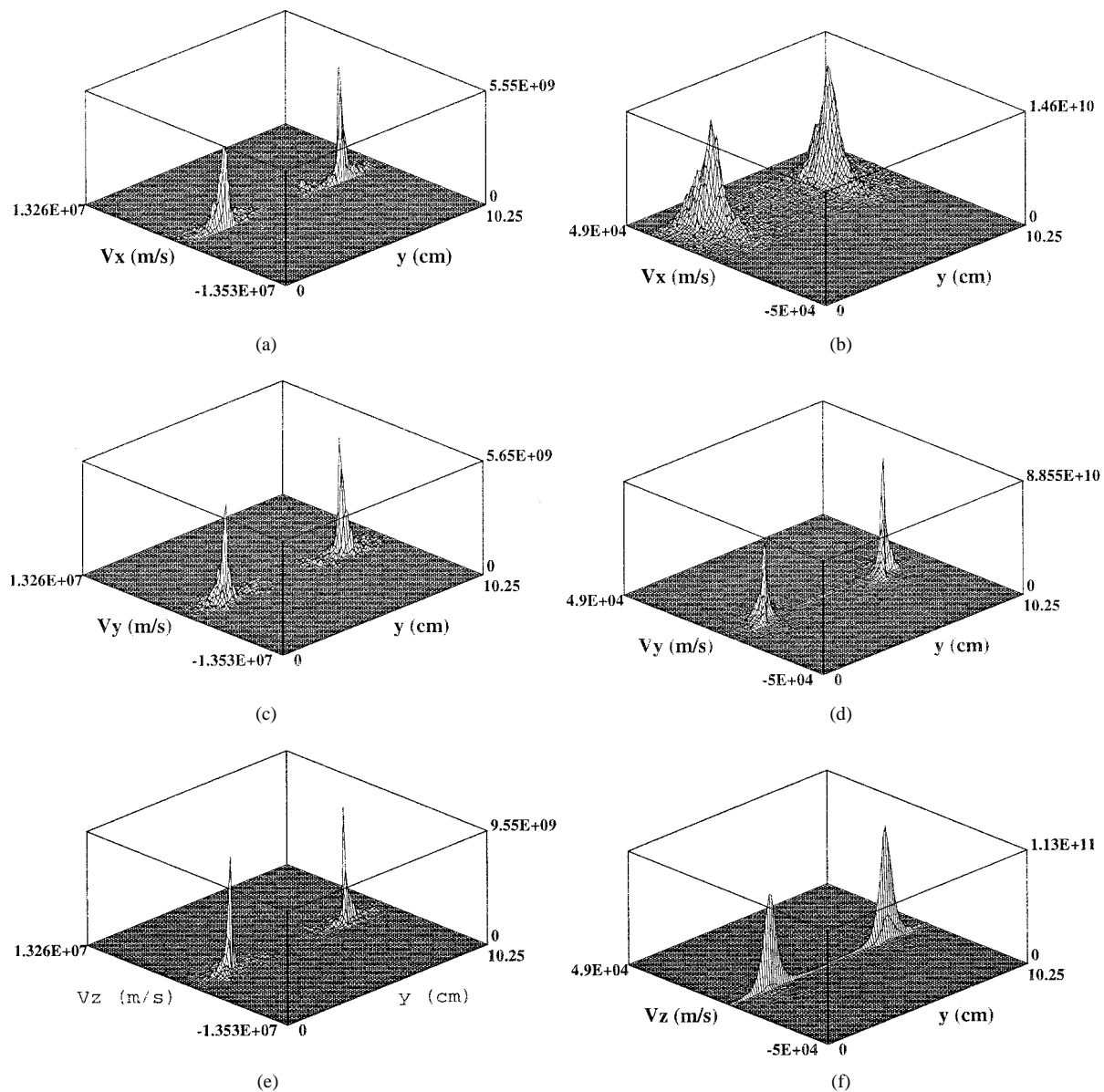


Fig. 9. Velocity distributions of electrons in (a) x , (c) y , (e) z direction, and ions in (b) x , (d) y , and (f) z direction at $t = 3 \times 10^{-6}$ s.

the cathode and at the density peak point. Points are the simulation results and the line is Maxwellian fitting. Electrons form a Maxwellian distribution. But ions are not well fitted to Maxwellian distribution function as shown in Figs. 12 and 13. Many particles are located in the high velocity tail. This result indicates that a particle simulation produces the results different from a fluid theory. There are hybrid, electron fluid-particle ion model [21], [22], and fluid modeling of bulk plasma [23]. Hybrid code simulation is used often to reduce simulation cost.

To clarify the particle distribution, we convert the velocity distribution to the energy distribution. Electron energy distribution is plotted in a semilog scale in Fig. 11. The data points are nearly on a straight line with one slope in the lower-energy region. In contrast to electron energy distribution, the ion energy distribution in Fig. 13 is not on a straight line. There are two kinds of fitting slopes. There

is a steep slope in the lower-energy region and another mild slope is in the high-energy region. This is consistent with the velocity-distribution profile. The high energy tail of velocity distribution corresponds to higher ion energy distribution.

As it is not easy to measure experimentally the low-energy particle distribution, this simulation can produce the results that elucidate the experimental situation. The energy of ions in the tail portion is high and contributes to high sputtering and cathode erosion. Therefore this simulation information is useful for experiments. The energy distribution of ions impinging on the cathode is crucial in determining the secondary emission of electrons as well as the sputtering and erosion rates. Our simulation shows that these ions with energy below 50 eV constitute the majority while these low-energy ions are rarely considered in measuring the secondary emission coefficient and the erosion rates.

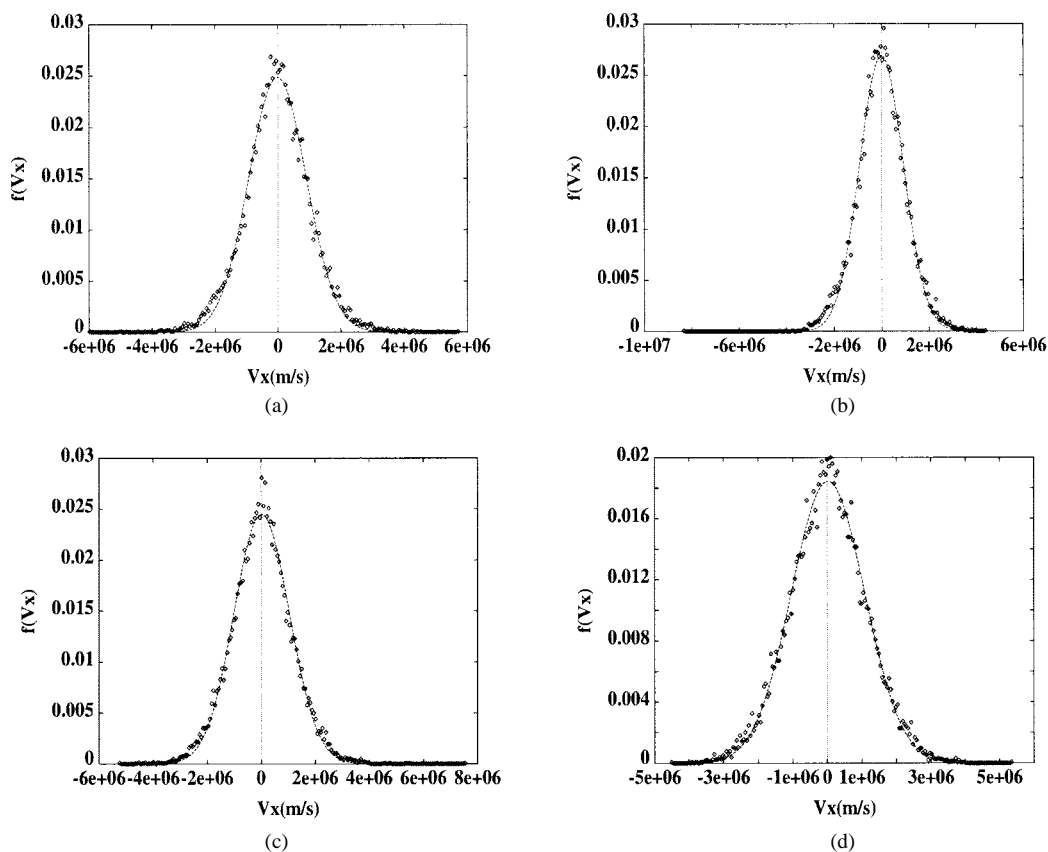


Fig. 10. X-direction velocity distributions of electrons (a) in front of cathode, (b) at the density peak-point at $t = 2 \times 10^{-6}$ s, (c) in front of cathode, and (d) at the density peak-point at $t = 3 \times 10^{-6}$ s.

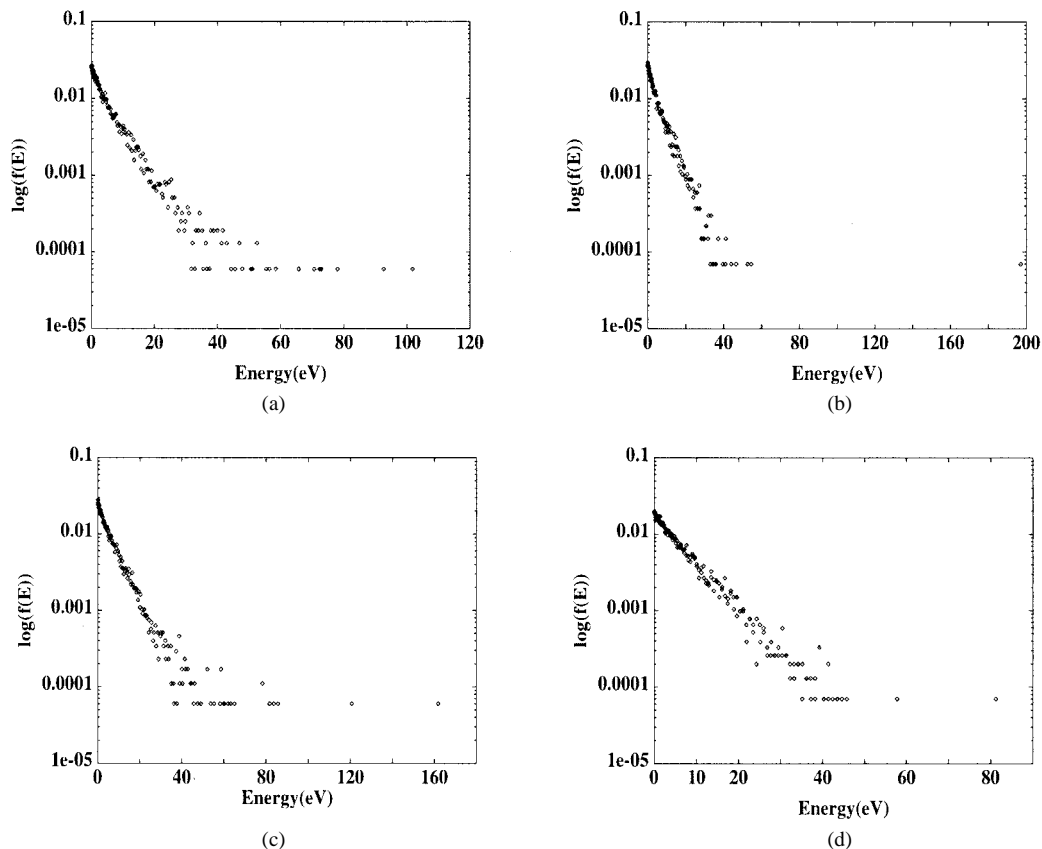


Fig. 11. X-direction electron energy distribution function (EEDF): (a) in front of cathode, (b) at the density peak-point at $t = 2 \times 10^{-6}$ s, (c) in front of cathode, and (d) at the density peak-point at $t = 3 \times 10^{-6}$ s. Y component is in a log scale.

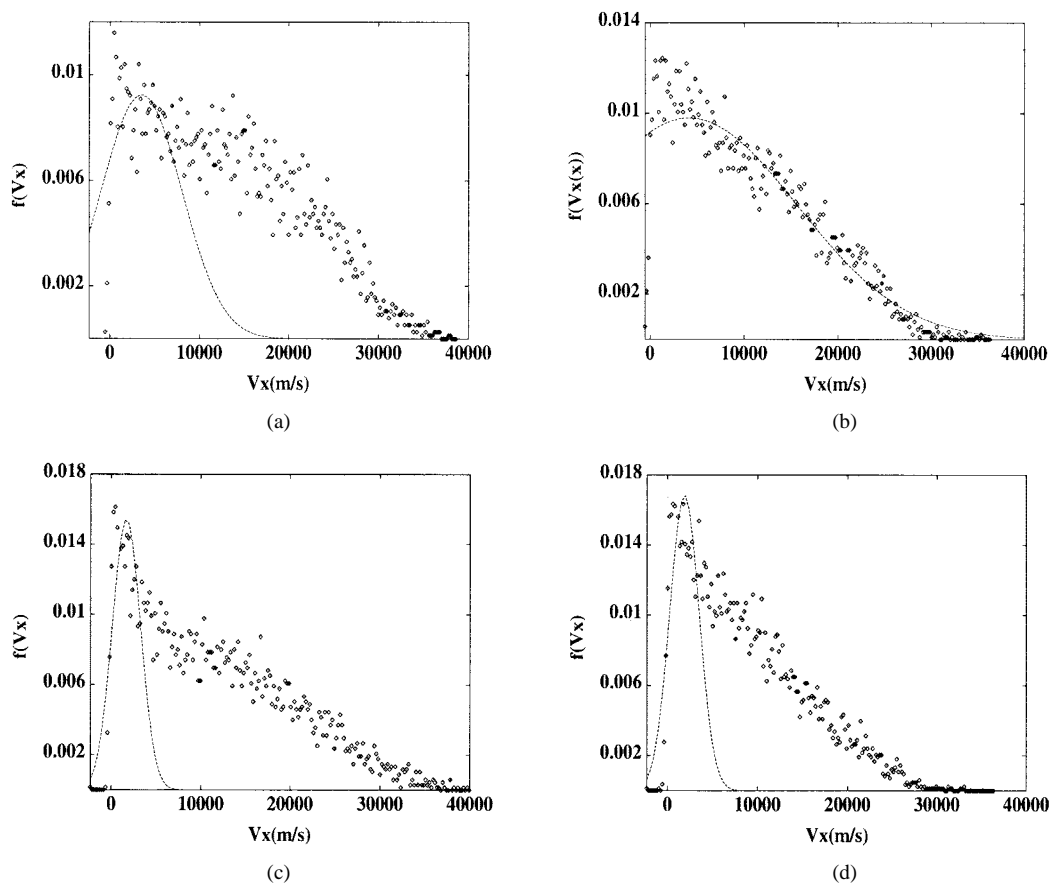


Fig. 12. X -direction velocity distributions of ions (a) in front of cathode, (b) at the density peak point at $t = 2 \times 10^{-6}$ s, (c) in front of cathode, and (d) at the density peak point at $t = 3 \times 10^{-6}$ s.

We also obtain the spatial electron and ion temperature distributions in Fig. 14. Electron temperature has nearly the same value of a few eV throughout the plasma-bulk region except for the sheath region where it is 20–25 eV, these values agree with the measurements [2], [3], and [24]. Temperature is around 5 eV in the bulk region, arising to 20–25 eV near the cathode. Near the cathode, the electron temperature is high and the starting point of temperature rising is associated with the sheath. The average electron temperature is approximately 5 eV in the bulk region at 3×10^{-6} s. Ion-temperature profiles show quite different characteristics. Ion temperature in the y direction does not vary much. But x or z direction temperature is increasing toward cathode. Especially, the x -direction temperature rapidly increases toward the anode. This particle-temperature profile is very important since incident ion temperature and direction are the quantities vitally related to surface reactions. The high ion energy yields high sputtering rate, which is linearly dependent on the ion temperature. The erosion profile is also dependent on the ion temperature. Energetic ions make larger erosion rates. The temperature of ions along the y direction is associated with the erosion profile.

In magnetron discharge, a fluid model has a limited applicability, because the operation pressure is order of mtorr. Especially in the sheath region, the plasma distribution is not Maxwellian. In Figs. 10–13, electrons are nearly Maxwellian,

while ions are not. Electron distribution also deviates from Maxwellian at the anode region. Ion distribution deviates from Maxwellian throughout the entire region. Thus a particle simulation produces results different from a fluid case.

Besides being a nonMaxwellian, the above results show that there are two kinds of distributions of ions. Ion energy distribution has two slopes. This is clearer in the 3×10^{-6} s result of Fig. 13(c) and (d). The high energy ions are important in magnetron device because these ions are engaged in sputtering, erosion, and secondary electron emission processes. In addition to high-energy ion distribution, we also obtain the low-energy ion distribution which forms the majority of ions near the cathode. It is not easy to measure experimentally the low-energy particle distribution and the surface reaction coefficients at the cathode for ions at very low energy (e.g., below 50 eV). Many ions have high energies but some components of ions are accelerated to the applied high voltage, causing the non-Maxwellian multitemperature distributions of ions. The mean free path is of an order of cm. Thus ions are accelerated without collision in the sheath. Our kinetic simulation has not reached a steady state due to a high computing cost; the information at the steady state can be obtained from Nanbu [8] and [9]. Our results, however, produce transient (but time-insensitive) profiles, especially the velocity distributions of ions near the cathode, which can be utilized effectively.

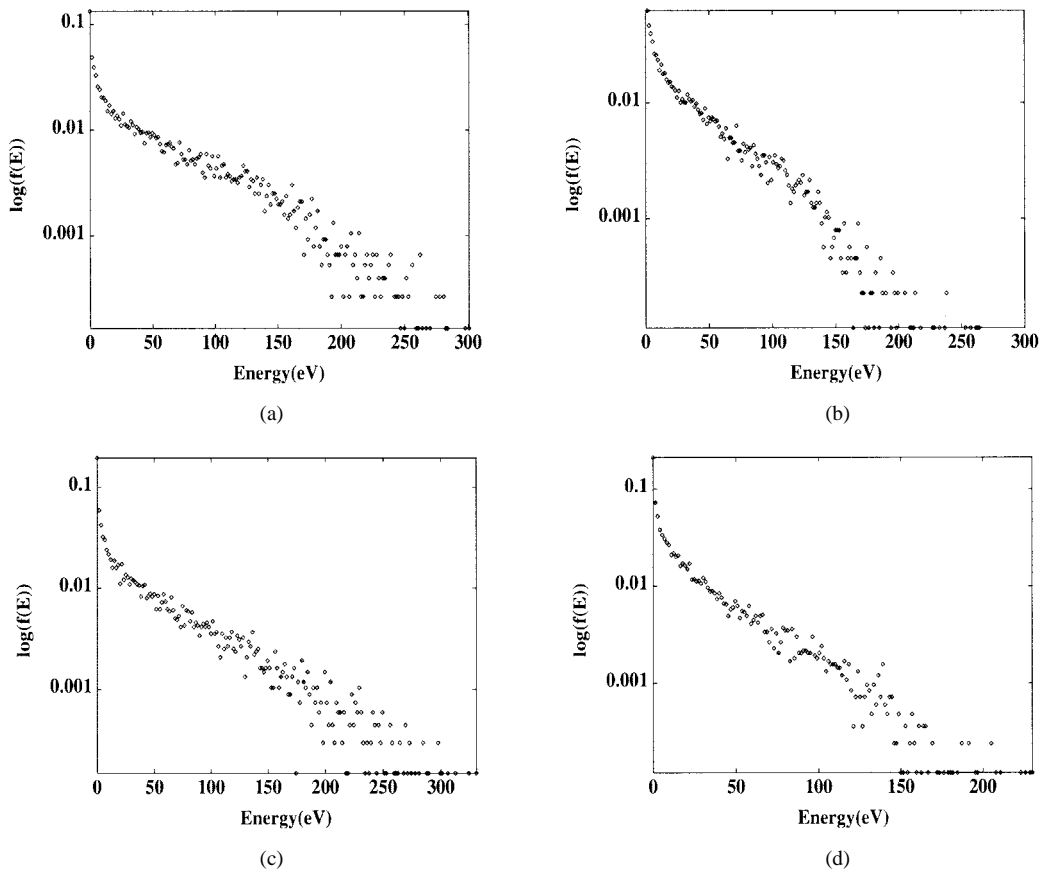


Fig. 13. X -direction energy distribution-function of ions (a) in front of cathode, (b) at the density peak point at $t = 2 \times 10^{-6}$ s, (c) in front of cathode, and (d) at the density peak-point at $t = 3 \times 10^{-6}$ s. Y component is in a log scale.

III. STEADY-STATE PROPERTY

In general the space-charge-limited current in a plane diode is given by the Child–Langmuir law [25]

$$\bar{J}_d = \frac{4\epsilon_0}{9} \sqrt{\frac{2e}{M}} \frac{V_c^{3/2}}{s^2} \quad (2)$$

where ϵ_0 is permittivity, e is particle charge, m is mass V_c is sheath voltage, s is sheath size.

Gu and Lieberman [1] and [5] proposed a new scaling

$$(s)_{GL} = C \frac{V^{7/8}}{I^{1/2} B^{1/4}} \quad (3)$$

and compared this with their optical emission measurement results. Although the experimental sheath size is almost twice higher than the value calculated from (3), the scaling of experimental sheath size with B agree well with Child's law. In this new equation they assumed that the total discharge current I is falling in the annulus of width \bar{w} , that is

$$I = \bar{A} \cdot \bar{J}_d = 2\pi r_0 \bar{w} \bar{J}_d \quad (4)$$

where \bar{A} is the mean area of the discharge, r_0 is the radius at which the magnetic field is tangent to the cathode surface, and \bar{w} is the mean width of the region of ion flux. In our simulation result, \bar{w} is approximately 1.5 cm which is shown in Fig. 5. Discharge \bar{A} is given by $2 \times \bar{w} = 3$ cm in this case. Current density is calculated using the result at the cathode in Fig. 9. The average current density \bar{J}_d is 62.22 (A/m²). Sheath size

determined from the (3) is 1.41 mm. The simulation sheath size, determined from potential and x - y particle distribution, is approximately 2 mm at 3×10^{-6} s, 1.8 mm at 3×10^{-6} s. These results have the same scaling with Gu and Lieberman's [1].

Gu and Lieberman's experimental condition $B = 342$ G, the voltage 396 V, the total current 0.5 A, produces the electron Larmor-radius $\lambda = 1.96$ mm, $(s)_{GL} = 1.23$ mm from (3), and the experimental sheath size $\Delta = 1.70$ mm. The magnetic field strength is taken on the cathode plate where the magnetic field is tangent to the cathode. These conditions are similar to our simulation condition $B = 302$ G, $V = 400$ V, which produces $\lambda = 2.23$ mm, and the total current 0.586 A, $(s)_{GL} = 1.41$ mm from (3), simulation sheath size $\Delta \approx 2$ mm. The above results show that the Larmor radius is close to the experimental sheath size rather than to $(s)_{GL}$.

Fujiyama [2], [3] replaced the sheath by an equivalent electron Larmor radius. These results are based on their ionization experiment. We estimated our steady state properties from Fujiyama formula because our simulation does not reach the steady state. In our case, the electron Larmor radius is approximately 2.23 mm, which is consistent with the simulation sheath size. Comparison between the experimental sheath of Gu and Lieberman and the electron Larmor radius yields the state-state current density. Power per unit z direction (1 m) is 2489 (W/m) in our simulation. The global model [26], [27] predicts that the current density is 216 (A/m²) from the

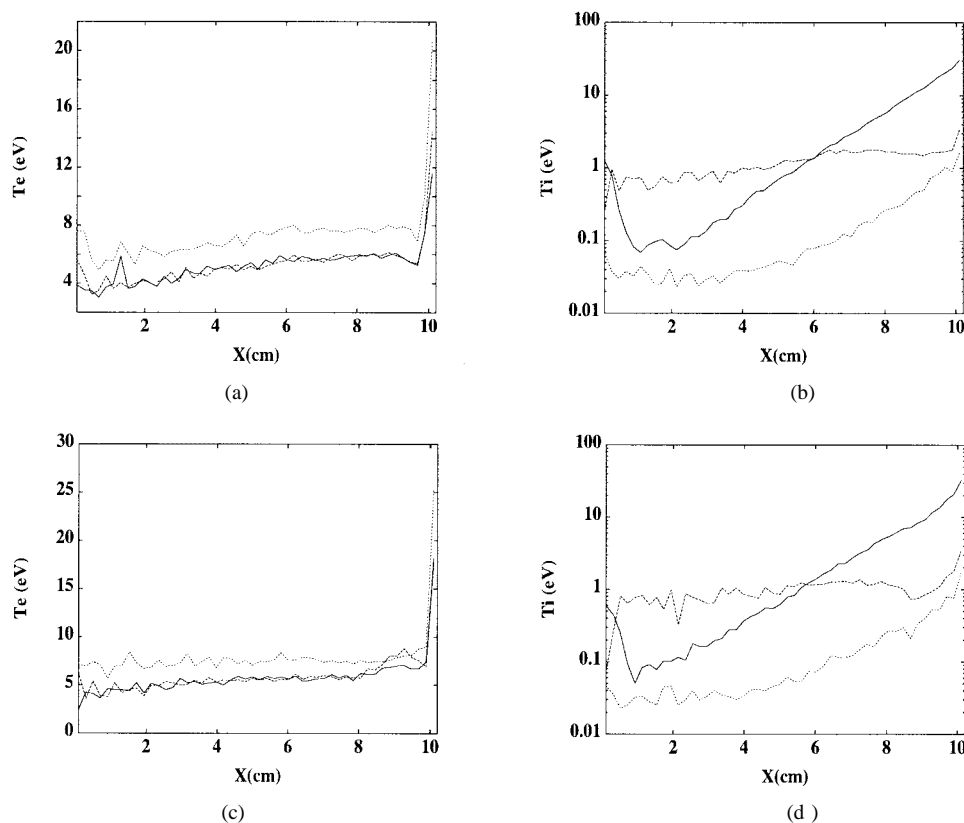


Fig. 14. Spatial temperature distributions of (a) electrons at $t = 2 \times 10^{-6}$ s, (b) ions at $t = 2 \times 10^{-6}$ s, (c) electrons at $t = 3 \times 10^{-6}$ s, and (d) ions at $t = 3 \times 10^{-6}$ s.

power obtained from the simulation result. This is consistent with the current density obtained from (2). Global model assumes a uniform magnetic field and a volume-averaged power. The discrepancy comes from the assumption of global model and the kinetic simulation is not carried out to reach a steady state.

We compared the 2-D magnetic field with 3-D magnetic field with a racetrack-type magnet. The 3-D magnetic field and the simulations (two space dimensions and three velocities) results with these fields are similar to the 2-D case near the linear section of the racetrack. Although there are some 3-D simulation results, they require much computing costs. The profiles in the linear section do not vary much except for the edge of the linear section [8] and [9]. Two-dimensional simulation can be used to optimize a magnetron geometry with low cost. The detail results with 3-D magnetic field are shown elsewhere.

IV. SUMMARY AND CONCLUSION

We simulate magnetron sputter by a particle code for plasma density and potential distribution along with current density distribution at the cathode. Electron and ion temperature profiles along x direction are obtained from simulation data. Ion-energy distribution is mostly in the lower energy range (below 50 eV) than that considered in the experimental measurements of the secondary emission coefficients and the erosion rates at the cathode. Kinetic simulation produces ion and electron velocity information related to deposition and

erosion profiles. Electron velocity distribution is Maxwellian except for the anode region. Ion profile is nonMaxwellian in the bulk and in the cathode sheath region. There are two different profiles of the energy distribution near the cathode.

ACKNOWLEDGMENT

The authors would like to thank Dr. Y. W. Choi, Y. S. Moon, and M. S. Hur for their helpful discussions.

REFERENCES

- [1] L. Gu and M. A. Lieberman, "Axial distribution of optical emission in a planar magnetron discharge," *J. Vac. Sci. Technol.*, vol. A6, no. 5, pp. 2960–2694, 1988.
- [2] K. Kuwahara and H. Fujiyama, "Applications of the Child–Langmuir law to magnetron discharge plasmas," *IEEE Trans. Plasma Sci.*, vol. 22, pp. 442–448, Aug. 1994.
- [3] ———, "Relation between plasma parameters and film properties in DC Reactive magnetron sputtering of ITO," *Jpn. J. Appl. Phys.*, vol. 36, no. 7B, pp. 4922–4927, 1997.
- [4] A. E. Wendt, M. A. Lieberman, and H. Meuth, "Radial current distribution at a planar magnetron cathode," *J. Vac. Sci. Technol.*, vol. A6, no. 3, pp. 1827–1831, 1988.
- [5] A. E. Wendt and M. A. Lieberman, "Spatial structure of a planar magnetron discharge," *J. Vac. Sci. Technol.*, vol. A8, no. 2, pp. 902–907, 1990.
- [6] Y. W. Choi, M. Bowden, and K. Muraoka, "A study of sheath electric fields in planar magnetron discharges using LIF spectroscopy," *Jpn. J. Appl. Phys.*, vol. 35, no. 11, pp. 5858–5861, 1996.
- [7] J. A. Thornton and A. S. Penfold, *Thin Film Processes*. New York: Academic, 1974, pp. 76–113.
- [8] K. Nanbu, S. Segawa, and S. Kondo, "Self-consistent particle simulation of 3-D DC magnetron discharge," *Vacuum*, vol. 47, no. 6–8, pp. 1013–1016, 1996.

- [9] K. Nanbu and S. Kondo, "Analysis of 3-D DC magnetron discharge by the particle-in-cell/Monte Carlo method," *Jpn. J. Appl. Phys.*, vol. 36, no. 7B, pp. 4808–4814, 1997.
- [10] C. K. Birdsall and A. B. Langdon, *Plasma Physics via Computer Simulation*. New York: McGraw-Hill, 1985.
- [11] J. H. Billen and L. M. Young, *Poisson Superfish*. Los Alamos, NM: Los Alamos National Lab., 1997.
- [12] F. F. Chen, *Introduction to Plasma Physics and Controlled Fusion*. New York: Plenum, 1984, pp. 30–34.
- [13] T. Motohiro and Y. Taga, "Monte Carlo simulation of thermalization process of sputtered particles," *Surf. Sci.*, vol. 134, pp. L494–L499, 1983.
- [14] T. Motohiro and Y. Taga, "Monte Carlo simulation of the particle transport process in sputter deposition," *Thin Solid Films*, vol. 112, pp. 161–173, 1984.
- [15] T. Motohiro, "Applications of Monte Carlo simulation in the analysis of a sputter-deposition," *J. Vac. Sci. Technol.*, vol. A4, no. 2, pp. 189–195, 1986.
- [16] R. R. Somekh, "The thermalization of energetic atoms during the sputtering process," *J. Vac. Sci. Technol.*, vol. A9, no. 3, pp. 688–690, 1991.
- [17] J. W. Bradley, "The plasma properties adjacent to the target in a magnetron sputtering source," *Plasma Sources Sci. Technol.*, vol. 5, pp. 622–631, 1996.
- [18] G. Lister, "Influence of electron diffusion on the cathode sheath of a magnetron discharge," *J. Vac. Sci. Technol.*, vol. A14, no. 5, pp. 2736–2743, 1996.
- [19] N. F. Cramer, "Analysis of a one-dimensional steady-state magnetron discharge," *J. Phys. D.*, vol. 30, pp. 2573–2584, 1996.
- [20] J. W. Bradley and G. Lister, "Model of the cathode fall region in magnetron discharges," *Plasma Sources Sci. Technol.*, vol. 6, pp. 524–532, 1997.
- [21] R. K. Porteous and D. B. Graves, "Modeling and simulation of magnetically confined low-pressure plasmas in two dimensions," *IEEE Trans. Plasma Sci.*, vol. 19, pp. 204–213, Apr. 1991.
- [22] R. K. Porteous, H.-M. Wu, and D. B. Graves, "A 2-D, axisymmetric model of a magnetized glow discharge plasma," *Plasma Sources Sci. Technol.*, vol. 3, pp. 25–39, 1993.
- [23] R. Krimke and H. M. Urbassek, "A fluid model of the bulk plasma in a cylindrical magnetized low-pressure RF discharge and comparison with PIC-MC simulation results," *Plasma Sources Sci. Technol.*, vol. 5, pp. 389–400, 1996.
- [24] S. M. Rosnagel and H. R. Kaufman, "Langmuir probe characterization of magnetron operation," *J. Vac. Sci. Technol.*, vol. A4, no. 3, pp. 1822–1825, 1986.
- [25] M. A. Lieberman and A. J. Lichtenberg, *Principles of Plasma Discharges and Materials Processing*. New York: Wiley, 1994.
- [26] J. K. Lee, L. Meng, Y. K. Shin, H. J. Lee, and T. H. Chung, "Modeling and simulation of a large-area plasma source," *Jpn. J. Appl. Phys.*, vol. 36, no. 9A, pp. 5714–5723, 1997.
- [27] H. J. Lee and J. K. Lee, "Time-dependent global model calculations for a pseudospark discharge with a hollow cathode," *Jpn. J. Appl. Phys.*, vol. 35, no. 12A, pp. 6252–6258, 1996.
- C. H. Shon**, photograph and biography not available at the time of publication.
- J. K. Lee**, photograph and biography not available at the time of publication.
- H. J. Lee**, photograph and biography not available at the time of publication.
- Y. Yang**, photograph and biography not available at the time of publication.
- T. H. Chung**, photograph and biography not available at the time of publication.